

# Nonlinear competition between asters and stripes in filament–motor–systems

Falko Ziebert and Walter Zimmermann

Theoretische Physik, Universität des Saarlandes, D-66041 Saarbrücken, Germany

the date of receipt and acceptance should be inserted later

**Abstract.** A model for polar filaments interacting via molecular motor complexes is investigated which exhibits bifurcations to spatial patterns. It is shown that the homogeneous distribution of filaments, such as actin or microtubules, may become either unstable with respect to an orientational instability of a finite wave number or with respect to modulations of the filament density, where long wavelength modes are amplified as well. Above threshold nonlinear interactions select either stripe patterns or periodic asters. The existence and stability ranges of each pattern close to threshold are predicted in terms of a weakly nonlinear perturbation analysis, which is confirmed by numerical simulations of the basic model equations. The two relevant parameters determining the bifurcation scenario of the model can be related to the concentrations of the active molecular motors and of the filaments respectively, which both could be easily regulated by the cell.

**PACS.** 87.16.-b Subcellular structure – 47.54.+r Pattern formation – 89.75.-k Complex systems

## 1 Introduction

In eukaryotic cells the polar filaments actin and microtubules interacting with motor proteins play a crucial role in intracellular organisation and transport as well as for the static and dynamical structure of the cytoskeleton [1, 2]. Most prominently, microtubules and kinesin are involved in highly connected dynamical structures, such as the mitotic spindle in cell division [3, 4], while the motility of the cell as a whole is governed by acto-myosin complexes [5, 6]. The dynamical behavior of such assemblies depends on the available biological fuel ATP (Adenosine-triphosphate), which is consumed during the motion of motor proteins along the filaments. Vesicles for instance are transported across a cell by motors moving along the tracks defined by microtubules, or – which is the scope of this work – oligomeric motor proteins that attach to two or more filaments induce relative motion between neighboring filaments and cause dynamical networks. The latter process is vitally important in cells, since the cytoskeleton constituted of the filaments has to be self-organized and even actively reorganized not only during cell-locomotion but also in order to react to outer stimuli (chemotaxis). During mitosis, microtubules attach to the chromosomes, which are then divided and the two halves finally are transported by the motor-induced filament sliding into the two evolving daughter cells.

Since the situation is very complex in a living cell, well designed in vitro experiments are the agent of choice for controlled explorations of prominent aspects of cellular systems. Recent experimental progress yielded indeed

important insights into organization and dynamical properties of the cell, which in turn call for modeling activities to foster their deeper understanding. These experiments comprise investigations of self-organization in filament–motor mixtures of microtubules in the presence of a single type of motor protein [7, 8, 9] and more recently also in actin–myosin networks [10, 11] as well as assays where two types of motors interact with microtubules [12]. Even in such model systems, simple compared to a living cell, there has been found a great variety of different two-dimensional patterns, such as stripe patterns, asters, vortices and irregular arrangements.

Works on modeling active filament–motor systems comprise molecular dynamics simulations [8, 12, 13] and mean field approximations for spin-like models displaying stripe-like patterns [14]. More recently a phenomenological model of a motor density interacting with a phenomenological vector field has been considered which is able to reproduce asters and vortex-like solutions [15] as well as models for bundle contraction in one spatial dimension [16, 17, 18].

Here we follow a more microscopic approach starting from the Smoluchowski equation for the spatial and angular distribution of rigid rods [19], which approximate the rather stiff microtubules and with limitations also the actin filaments. It is well known since Onsager’s theory that an ideal rigid rod system exhibits a nematic liquid crystalline order beyond some critical rod density [20, 21] which is still present in generalizations for semiflexible polymers, albeit at a slightly higher filament density [22], and has been observed in vitro for both kinds of biopolymers [23, 24]. To use Onsager’s equilibrium argument of

excluded volume induced transitions in a nonequilibrium system like the cell, one can formulate phenomenological models as done recently to describe how nucleation and decay of the filaments in a cell at a density close to the isotropic–nematic transition may give rise to spatially periodic patterns [25]. Alternatively one can use the aforementioned Smoluchowski equation for rigid rods [19], which is an approach widely used in polymer and colloidal science and recently has been supplemented by active currents to describe filament–motor–systems [26] in a way inspired by a macroscopic model for filament bundling in one spatial dimension [17]. In this approach one makes use of the fact that the small motor proteins diffuse much faster than the filaments. Hence the density of the motors can be assumed to be homogeneous and – as well as properties like the mean velocity and the duty ratio of the motors – enters into the model only via the coefficients. The phenomenological description of the active currents can be derived by symmetry considerations and includes three major contributions, whereof in this work we focus on the effects on pattern formation of only two of them. Since most of the experimental assays are quasi two-dimensional, we restrict our analysis also to two spatial dimensions.

The filament–filament interactions induced by the motors as well as by excluded volume effects are nonlocal. Thus they have to be approximated by a gradient expansion, which must not be truncated at the leading order, because on their basis the instabilities of the homogeneous filament distributions cannot be predicted as pointed out recently [27], but has to be continued up to fourth order derivatives. Since in vitro aster-like patterns evolve at much lower filament density than the isotropic–nematic transition, a moment expansion of the probability density function can be truncated to derive a closed set of equations for the physical observables, which are the density and the orientation field of the filaments. After a detailed linear analysis the major goal of this work is a characterization of the nonlinear behavior of patterns beyond their threshold. For this purpose we employ on the one hand numerical simulations of the coupled equations for the filament density and the orientational field. On the other hand we use the powerful method of amplitude expansion, where equations of motion for the amplitudes of the spatially periodic pattern are derived close to the pattern forming instability [28, 29, 30].

The generic patterns in two–dimensional systems close to threshold are stripes, squares or hexagonal patterns and for the amplitudes of these patterns generic nonlinear amplitude equations may be derived [28, 31]. In numerical simulations we found either stripes or squares (the absence of hexagonal structures can be explained by the hierarchy of equations in the derivation of the amplitude equation) and therefore we focus on the equations for stripe and square patterns (as described by Eq. (27) below), which are of the form [28, 32]

$$\tau_0 \partial_t X = \varepsilon X - g_1 |X|^2 X - g_2 |Y|^2 X , \quad (1a)$$

$$\tau_0 \partial_t Y = \varepsilon Y - g_1 |Y|^2 Y - g_2 |X|^2 Y . \quad (1b)$$

Here  $\varepsilon$  denotes the deviation of the control parameter from its value at the threshold of pattern formation, while  $X$  and  $Y$  describe the amplitudes of a spatially periodic pattern in one (stripe) or two orthogonal directions (square), namely the  $x$ - and  $y$ -direction. These amplitude equations are universal for all pattern forming systems of a given symmetry and the specific information of each system is only encoded in the coefficients, namely  $\tau_0, g_1, g_2$ , which are functions of the parameters of the underlying system under consideration. The nonlinear analysis of Eqs. (1) is worked out analytically and by this advantage a whole phase diagram for the various patterns close to threshold is presented. In contrast, such an investigation would be very cumbersome and time consuming using numerical simulations of the model equations. The solution  $|X| = |Y|$  corresponds to a square pattern for the orientational field of the filaments which resembles very much a structure of periodically arranged asters.

The work is organized as follows. The underlying microscopic model for the filament distribution is presented in Sec. 2 and in the same section we derive also the coupled equations for the density and orientation of the filaments, whereby the technical parts are moved to the appendices. The thresholds of the pattern forming instabilities and its dependence of the parameters are determined in section 3, where we find an instability leading to density modulations, an orientational instability as well as a liquid-crystalline isotropic–nematic (I–N) transition. With regard to the formation of asters, the orientational instability is the most interesting one and its nonlinear behavior, namely the nonlinear stripe solutions and the periodic lattice of asters and inverse asters as well as their stability are investigated in more detail in Secs. 4 and 5. The work is finished with a summary and concluding remarks.

## 2 The model

The probability of finding a rod (with fixed length  $L$ ) at the position  $\mathbf{r}$  with the orientation  $\mathbf{u}$  (with  $|\mathbf{u}| = 1$ ) at time  $t$  is described by the distribution function  $\Psi(\mathbf{r}, \mathbf{u}, t)$ <sup>1</sup> and the governing so-called Smoluchowski equation is just the continuity equation for the probability

$$\partial_t \Psi + \nabla \cdot \mathbf{J}_t + \mathcal{R} \cdot \mathbf{J}_r = 0 . \quad (2)$$

Homogeneously distributed molecular motors are supposed to interact with the rods inducing active currents on them. The total translational and rotational currents are given in Cartesian coordinates by

$$\mathbf{J}_{t,i} = -D_{ij} [\partial_j \Psi + \Psi \partial_j V_{ex}] + J_{t,i}^a , \quad (3a)$$

$$\mathbf{J}_{r,i} = -D_r [\mathcal{R}_i \Psi + \Psi \mathcal{R}_i V_{ex}] + J_{r,i}^a . \quad (3b)$$

The terms with an upper index  $a$  are the motor–mediated active currents, the translational diffusion matrix reads

$$D_{ij} = D_{\parallel} u_i u_j + D_{\perp} (\delta_{ij} - u_i u_j) , \quad (4)$$

<sup>1</sup> In the following we will write  $\Psi(\mathbf{r}, \mathbf{u})$  for reasons of brevity and  $\Psi(\mathbf{r}, \mathbf{u}, t)$  only if we want to emphasize the time dependence.

$D_r$  is the rotational diffusion constant and the operator of rotational diffusion is given by

$$\mathcal{R} = \mathbf{u} \times \partial_{\mathbf{u}} . \quad (5)$$

$V_{ex}$  describes the excluded volume interaction

$$V_{ex}(\mathbf{r}, \mathbf{u}) = \int d\mathbf{u}' \int d\mathbf{r}' W(\mathbf{r}-\mathbf{r}', \mathbf{u}, \mathbf{u}') \Psi(\mathbf{r}', \mathbf{u}') \quad (6)$$

between rods, where the interaction kernel is expressed in terms of the so-called Straley coordinates  $\zeta$  and  $\eta$  in two dimensions [33]

$$W(\mathbf{r}-\mathbf{r}', \mathbf{u}, \mathbf{u}') = |\mathbf{u} \times \mathbf{u}'| \int_{-L/2}^{L/2} d\zeta \int_{-L/2}^{L/2} d\eta \delta(\mathbf{r}-\mathbf{r}'+\mathbf{u}\zeta+\mathbf{u}'\eta) . \quad (7)$$

This expression takes into account that there is only an interaction between rods with coordinates  $(\mathbf{r}, \mathbf{u})$  and  $(\mathbf{r}', \mathbf{u}')$  in the case of a finite overlap i.e. if the connection vector  $\mathbf{r}-\mathbf{r}'$  can be constructed by a linear combination  $\mathbf{u}\zeta+\mathbf{u}'\eta$  of the rod orientations with  $-L/2 < \zeta, \eta < L/2$ . The active currents induced by the homogeneous motor density are

$$\begin{aligned} J_t^a &= \Psi(\mathbf{r}, \mathbf{u}) \int d\mathbf{u}' \int d\mathbf{r}' \mathbf{v}(\mathbf{r}-\mathbf{r}', \mathbf{u}, \mathbf{u}') W(\mathbf{r}-\mathbf{r}', \mathbf{u}, \mathbf{u}') \Psi(\mathbf{r}', \mathbf{u}') , \\ J_r^a &= \Psi(\mathbf{r}, \mathbf{u}) \int d\mathbf{u}' \int d\mathbf{r}' \boldsymbol{\omega}(\mathbf{u}, \mathbf{u}') W(\mathbf{r}-\mathbf{r}', \mathbf{u}, \mathbf{u}') \Psi(\mathbf{r}', \mathbf{u}') \end{aligned} \quad (8)$$

with the translational and rotational velocity given by

$$\mathbf{v}(\mathbf{r}-\mathbf{r}', \mathbf{u}, \mathbf{u}') = \frac{\alpha}{2} \frac{\mathbf{r}-\mathbf{r}'}{L} \frac{1+\mathbf{u} \cdot \mathbf{u}'}{|\mathbf{u} \times \mathbf{u}'|} + \frac{\beta}{2} \frac{\mathbf{u}' - \mathbf{u}}{|\mathbf{u} \times \mathbf{u}'|} , \quad (9)$$

$$\boldsymbol{\omega}(\mathbf{u}, \mathbf{u}') = \gamma(\mathbf{u} \cdot \mathbf{u}') \frac{\mathbf{u} \times \mathbf{u}'}{|\mathbf{u} \times \mathbf{u}'|} , \quad (10)$$

respectively. The active currents are normalized to the interaction volume and they fulfill both, the conservation of translational and rotational momentum in the absence of external forces and torques, as well as translational and rotational invariance (c.f. [26] and appendix A).

According to its functional dependence  $1+\mathbf{u} \cdot \mathbf{u}'$ , the first term in Eq. (9) contributes at maximum to the filament transport for a parallel orientation, which identifies it as the leading pattern forming mechanism in counteraction with the diffusive motion. It arises from a difference in motor activity between the filament center and the filament endpoints, where motors stall for some finite time  $\tau_f$ , which has been recognised as a crucial condition for aster formation [34]. It depends also on the relative filament separation  $\mathbf{r}-\mathbf{r}'$ , hence no relative motion is obtained if the motor connects two filaments having the same centers of mass.

The second term in Eq. (9), proportional to  $\beta$ , causes filament translations along  $\mathbf{u}'-\mathbf{u}$  and therefore becomes maximal for antiparallel filament orientations. The contribution in Eq. (10) causes rotational currents. In this work we focus mainly on active currents caused by the  $\alpha$ -term

and especially on its effects on pattern formation in two spatial dimensions.

Eq. (2) together with the currents as defined by Eqs. (3) and (8) cannot be solved analytically for  $\Psi(\mathbf{r}, \mathbf{u}, t)$  and even numerically, being a nonlinear integro-differential equation, it would be rather intricate. However, these equations may be simplified by expressing the distribution function in terms of its moments. For a rod distribution, the zeroth, first and second moment with respect to the orientation correspond to the filament density  $\rho(\mathbf{r}, t)$ , the polar orientation  $\mathbf{t}(\mathbf{r}, t)$  and the nematic order parameter  $S_{ij}(\mathbf{r}, t)$ , which are defined by the following expressions

$$\begin{aligned} \rho(\mathbf{r}, t) &= \int d\mathbf{u} \Psi(\mathbf{r}, \mathbf{u}, t) , \\ \mathbf{t}(\mathbf{r}, t) &= \int d\mathbf{u} \mathbf{u} \Psi(\mathbf{r}, \mathbf{u}, t) , \\ S_{ij}(\mathbf{r}, t) &= \int d\mathbf{u} u_i u_j \Psi(\mathbf{r}, \mathbf{u}, t) . \end{aligned} \quad (11)$$

In contrast to a usual lyotropic liquid crystal [20], here the filaments are polar with respect to the motor action which breaks the  $\pm\mathbf{u}$ -symmetry and therefore the first moment may become finite.

The critical filament density of the homogeneous isotropic-nematic (I-N) transition can be determined by the stability of the second moment of the rotational diffusion contribution, i.e. where  $-D_r \int u_\alpha u_\beta \mathcal{R} [\mathcal{R}\Psi + \Psi\mathcal{R}V_{ex}]$  changes its sign. This condition yields the critical density

$$\rho_{IN} = \frac{3}{2}\pi \quad (12)$$

in two spatial dimensions where the I-N transition is of second order.

In order to obtain a closed set of equations of motion, the distribution function  $\Psi(\mathbf{r}, \mathbf{u}, t)$  may be expanded with respect to the leading moments as given by Eqs. (11). In the parameter range well below the homogeneous I-N transition, where aster formation is observed in vitro and on which we concentrate in this work, the first two moments are sufficient and the distribution function may be represented in terms of  $\rho(\mathbf{r}, t)$  and  $\mathbf{t}(\mathbf{r}, t)$  (for more details we refer to appendix C)

$$\Psi(\mathbf{r}, \mathbf{u}, t) = \frac{1}{2\pi} (\rho(\mathbf{r}, t) + 2\mathbf{u} \cdot \mathbf{t}(\mathbf{r}, t)) . \quad (13)$$

To get rid of the integral kernel in Eq. (7), a gradient expansion can be performed as described in more detail in appendix B. After a rescaling of variables via

$$\begin{aligned} t' &= \frac{D_{\parallel}}{l^2} t , \quad x' = \frac{1}{l} x , \quad \rho' = v_0 \rho , \quad \mathbf{t}' = v_0 \mathbf{t} , \\ \alpha' &= \frac{l}{D_{\parallel}} \alpha , \quad D_r' = \frac{l^2}{D_{\parallel}} D_r , \quad d = \frac{D_{\perp}}{D_{\parallel}} = \frac{1}{2} , \end{aligned} \quad (14)$$

where for the last relation we refer to [19], we obtain in two spatial dimensions the following coupled equations for the

density and the two components of the polar orientation field  $t_i$  ( $i = x, y$ ) of the filaments

$$\begin{aligned} \partial_t \rho = & \frac{3}{4} \Delta \rho + \left[ \frac{3}{2\pi} - \frac{\alpha}{24} \right] \nabla \cdot (\rho \nabla \rho) \\ & - \frac{\alpha}{48} \partial_i \left[ t_i \partial_j t_j + t_j \partial_i t_j + t_j \partial_j t_i \right] \\ & - \frac{\alpha}{C_1} \left\{ 38 \nabla \cdot (\rho \nabla \Delta \rho) + 11 \partial_i (t_j \partial_i \Delta t_j) \right. \\ & \left. + 16 \partial_i \left[ t_i \Delta \partial_j t_j + 2 t_j \partial_j \partial_i \partial_l t_l + t_j \partial_j \Delta t_i \right] \right\}, \end{aligned} \quad (15a)$$

$$\begin{aligned} \partial_t t_i = & -D_r t_i + \frac{5}{8} \Delta t_i + \frac{1}{4} \partial_i \nabla \cdot \mathbf{t} \\ & + \frac{1}{4\pi} \left[ 5 \partial_j (t_i \partial_j \rho) + \partial_j (t_j \partial_i \rho) + \partial_i (t_j \partial_j \rho) \right] \\ & - \frac{\alpha}{96} \partial_j \left[ 3 t_i \partial_j \rho + t_j \partial_i \rho + \rho (\partial_i t_j + \partial_j t_i) \right] \\ & - \frac{\alpha}{96} \partial_i \left[ t_i \partial_l \rho + \rho \partial_l t_i \right] - \frac{16\alpha}{C_2} \partial_i \left[ \rho \Delta \partial_l t_l + t_l \partial_l \Delta \rho \right] \\ & - \frac{\alpha}{C_2} \partial_j \left[ \rho \left( 11 \partial_j \Delta t_i + 16 \partial_i \Delta t_j + 32 \partial_j \partial_i \partial_l t_l \right) \right. \\ & \left. + 16 t_j \partial_i \Delta \rho + 32 t_l \partial_l \partial_i \partial_j \rho + 44 t_i \partial_j \Delta \rho \right] \\ & + \frac{1}{48} \left[ \frac{\gamma}{4} - \frac{4}{\pi} D_r \right] \left\{ t_j \partial_j \partial_i \rho - \frac{1}{2} t_i \Delta \rho \right\} \end{aligned} \quad (15b)$$

with  $C_1 = 23040$  and  $C_2 = 2C_1$ .

The contributions to Eqs. (15) that include also fourth order derivatives are crucial for the determination of the instabilities evolving from the homogeneous filament distribution and the nonlinear patterns in the following sections. Their importance was pointed out recently in a comment [27] on a previous work [26]. It should be noted that fourth order derivatives proportional to the translational diffusion have been neglected here because they are over-compensated by the fourth derivatives resulting from the active current and therefore influence the presented results only quantitatively by a small amount (but considerably complicate the equations).

The instabilities of the homogeneous filament distribution caused by the  $\alpha$ -contribution to the active current, c.f. (9,10), and the nonlinear solutions are determined in the following sections. The active current proportional to  $\beta$  leads to additional effects, which are responsible e.g. for propagating modes in the system and for the breaking of the unexpected  $\mathbf{t} \rightarrow -\mathbf{t}$  symmetry of Eqs. (15). To remind the reader, we have allowed  $\mathbf{t}$  to become nonzero, so we allowed the breaking of the  $\pm \mathbf{u}$ -symmetry of Eq. (2), but our model equations (15) nevertheless have a  $\pm \mathbf{t}$ -symmetry, since terms like  $\mathbf{t}^2$  appear in the equation for  $\mathbf{t}$  only due to the  $\beta$ -contribution of the current. These effects are determined elsewhere [35] and the corresponding contributions to Eqs. (15) are not shown for the sake of brevity. The active rotational current proportional to  $\gamma$  is nonlinear and

therefore influences only the nonlinear behavior of pattern selection beyond threshold as shown briefly in Sec. 4.

### 3 Threshold for density and orientational instabilities

Having defined the model, the first issue in the field of pattern formation is the determination of possible instabilities. As calculated in this section by a linear stability analysis, in a certain parameter range the homogeneous basic state, which consists here in a constant filament density  $\rho_0$  and a vanishing polar orientation  $\mathbf{t} = 0$ , becomes unstable with respect to inhomogeneous perturbations  $\tilde{\rho}(\mathbf{r}, t)$  and  $\mathbf{t}(\mathbf{r}, t)$ . For this purpose, by the ansatz  $\rho(\mathbf{r}, t) = \rho_0 + \tilde{\rho}(\mathbf{r}, t)$  we separate the constant part  $\rho_0$  of the filament density from the spatially inhomogeneous one,  $\tilde{\rho}(\mathbf{r}, t)$ , and linearize Eqs. (15) with respect to small inhomogeneous contributions  $\tilde{\rho}(\mathbf{r}, t)$  and  $\mathbf{t}(\mathbf{r}, t)$ . Accordingly a set of three coupled linear equations is obtained

$$\partial_t \mathbf{w}(\mathbf{r}, t) = \mathcal{L}_0 \mathbf{w}(\mathbf{r}, t) = \begin{pmatrix} \mathcal{L}_{11}^{(0)} & 0 & 0 \\ 0 & \mathcal{L}_{22}^{(0)} & \mathcal{L}_{23}^{(0)} \\ 0 & \mathcal{L}_{32}^{(0)} & \mathcal{L}_{33}^{(0)} \end{pmatrix} \mathbf{w}(\mathbf{r}, t), \quad (16)$$

for the three components of the vector

$$\mathbf{w}(\mathbf{r}, t) = \begin{pmatrix} \tilde{\rho} \\ t_x \\ t_y \end{pmatrix} (\mathbf{r}, t). \quad (17)$$

The components of the linear operator  $\mathcal{L}_0$  are given by the expressions

$$\begin{aligned} \mathcal{L}_{11}^{(0)} &= \left[ \frac{3}{4} \left( 1 + \frac{2}{\pi} \rho_0 \right) - \frac{\alpha \rho_0}{24} \right] \Delta - \frac{19 \alpha \rho_0}{11520} \Delta^2, \\ \mathcal{L}_{22}^{(0)} &= -D_r + \frac{5}{8} \Delta + \frac{1}{4} \partial_x^2 - \frac{\alpha \rho_0}{96} (\Delta + 2 \partial_x^2) \\ &\quad - \frac{\alpha \rho_0}{46080} (11 \Delta^2 + 64 \Delta \partial_x^2), \\ \mathcal{L}_{23}^{(0)} &= \left( \frac{1}{4} - \frac{\alpha \rho_0}{48} \right) \partial_x \partial_y - \frac{\alpha \rho_0}{720} \Delta \partial_x \partial_y \end{aligned} \quad (18)$$

and the two further components  $\mathcal{L}_{32}^{(0)}$  and  $\mathcal{L}_{33}^{(0)}$  may be obtained by permuting  $\partial_x$  and  $\partial_y$  in  $\mathcal{L}_{23}^{(0)}$  and  $\mathcal{L}_{22}^{(0)}$ , respectively. Naturally the mode ansatz

$$\mathbf{w}(\mathbf{r}, t) = \mathbf{E} \exp(\sigma t + i \mathbf{k} \cdot \mathbf{r}) \quad (19)$$

with the wave vector  $\mathbf{k} = (q, p)$  and the eigenvector  $\mathbf{E}$  solves the linear homogeneous set of equations (16) and the solubility condition provides a third order polynomial for the eigenvalue  $\sigma$ , which factorizes into a linear and a quadratic polynomial describing different types of instabilities. Considering moderate filament densities, for intermediate values of  $\alpha$ , an orientational instability with a finite wavelength is preferred, whereas the density mode does not couple on the level of the linear equations. For

large values of  $\alpha$  a further mode becomes unstable which resembles a spinodal decomposition of the filament density driven by the motor proteins.

The latter instability with respect to density fluctuations is governed by  $\mathcal{L}_{11}^{(0)}$  and the eigenvalue

$$\sigma_d = -\left[\frac{3}{4}\left(1 + \frac{2}{\pi}\rho_0\right) - \frac{\alpha\rho_0}{24}\right]k^2 - \frac{19}{11520}\alpha\rho_0 k^4 \quad (20)$$

with  $k^2 = q^2 + p^2$ . The term  $\propto k^4$  is always stabilizing, but the homogeneous basic state becomes unstable with respect to density modulations for a positive coefficient of  $k^2$  leading to the corresponding critical filament density

$$\rho_d = \frac{1}{\frac{\alpha}{18} - \frac{2}{\pi}} \quad (21)$$

providing that  $\alpha > \frac{36}{\pi}$  holds. The corresponding eigenvector is  $\mathbf{E}_d = (1, 0, 0)^T$  and the dispersion is shown as the dotted lines in Fig. 1a) and b) for subcritical and supercritical values respectively.

Of the remaining two eigenvalues,  $\sigma_I$  and  $\sigma_S$ , only the first may become positive in a finite range of  $k$  as indicated by the solid lines in Fig. 1. It describes an instability with respect to orientational fluctuations with the dispersion relation

$$\sigma_I = -D_r - \frac{1}{4}k^2\left(\frac{7}{2} - \frac{\alpha\rho_0}{8} + \frac{5}{768}\alpha\rho_0 k^2\right), \quad (22)$$

while  $\sigma_S$ , shown as the dashed lines in Fig. 1, is always damped and related to diffusion of orientational modes. The two corresponding eigenvectors are

$$\mathbf{E}_I = \begin{pmatrix} 0 \\ q \\ p \end{pmatrix}, \quad \mathbf{E}_S = \begin{pmatrix} 0 \\ q \\ -p \end{pmatrix}. \quad (23)$$

It should be mentioned that the eigenvalues  $\sigma_d(k)$ ,  $\sigma_I(k)$ ,  $\sigma_S(k)$  depend only on even powers of the wave number modulus reflecting the rotational symmetry of the basic state  $(\rho_0, \mathbf{t})$ . The restabilizing  $k^4$ -term in Eq. (22) was missing in Ref. [26], as pointed out recently [27]. However, only the interplay between the  $k^2$  and  $k^4$  contribution as in Eq. (22) allows the identification of a finite wavenumber instability. The extremal condition together with the neutral stability condition

$$\left.\frac{d\sigma_I}{dk}\right|_{k_c} = 0, \quad \sigma_I(k = k_c) = 0, \quad (24)$$

allow the determination of the critical filament density  $\rho_c$  at the critical wavenumber  $k_c$ , above which the orientational instability takes place:

$$\rho_c = \frac{1}{\alpha} \left(28 + \frac{10}{3}D_r \left(1 + \sqrt{1 + \frac{84}{5D_r}}\right)\right), \quad (25)$$

$$k_c = 4 \left(\frac{12D_r}{5\alpha\rho_c}\right)^{1/4}. \quad (26)$$

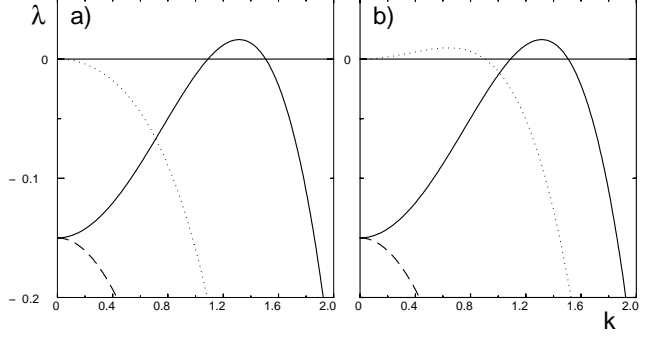


**Fig. 1.** The real parts  $\lambda(k) = \text{Re}[\sigma(k)]$  of the eigenvalue  $\sigma_d$  corresponding to the instability with respect to density fluctuations (dotted line) as well as the one with respect to orientational fluctuations,  $\sigma_I$  (solid line), are shown as a function of the wave number  $k$  for  $D_r = 0.15$ . The third eigenvalue  $\sigma_S$  is always damped as depicted by the dashed line. In part a) we have chosen  $\alpha = 21$  and therefore  $\rho_c < \rho_0 < \rho_d$  leading to an orientational instability, whereas in part b) one has  $\alpha = 26$  and  $\rho_d < \rho_c < \rho_0$ , hence both modes  $\sigma_d$  and  $\sigma_I$  have positive real parts in a finite wave number range (see also Fig. 2).

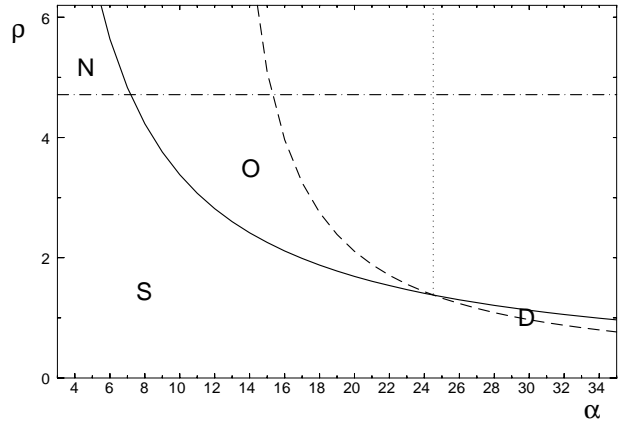


**Fig. 2.** The critical densities  $\rho_c$  (solid line) and  $\rho_d$  (dashed line) for the orientational and density instability respectively are shown as a function of  $\alpha$  and for  $D_r = 0.15$ . The dash-dotted horizontal line is the critical density  $\rho_{IN} = \frac{3}{2}\pi$ , above which the isotropic–nematic transition due to excluded volume interactions takes place. In the range referred to as  $N$  one has a pure homogeneous transition to nematic order, in range  $O$  one has a motor driven spatially periodic orientational order and in range  $D$  one has modulations of the filament density. The region  $S$  denotes the parameter range where the homogeneous solution is stable. In the following sections of the paper we investigate the nonlinear behavior in the  $O$ -region.

Fig. 1 displays the dispersions, i.e. the wavenumber dependent growth rates,  $\sigma_d(k)$ ,  $\sigma_I(k)$  and  $\sigma_S(k)$  as dotted, solid and dashed lines respectively. In Fig. 2, the critical density  $\rho_d$  (dashed line) for an instability with respect to inhomogeneous density fluctuations and  $\rho_c$  (solid line) with respect to inhomogeneous orientational fluctuations  $\mathbf{t}(\mathbf{r}, t)$  are shown as a function of motor activity  $\alpha$ . The dash-dotted line describes the critical density  $\rho_{IN}$  (12)

above which the homogeneous isotropic–nematic transition takes place. On the left side of the dotted line, orientational fluctuations have lowest threshold, while on the right side density fluctuations become unstable at first. For increasing values of the rotational diffusion coefficient  $D_r$ , which determines how negative the dispersions  $\sigma_I(k)$  and  $\sigma_S(k)$  start from  $k = 0$ , the solid line is shifted upwards in Fig. 2 decreasing the  $\alpha$ -range wherein the orientational instability has lowest threshold with  $\rho_c < \rho_{IN}$ .

Beyond some critical value of  $\beta$ , the  $\beta$ -contribution to the active current (8,9) induces an oscillatory bifurcation from the homogeneous filament distribution as described in a forthcoming work, where also the nonlinear behavior of the oscillatory patterns is discussed [35]. The contribution of the rotational current (8,10) to Eqs. (15) includes only nonlinear terms and therefore does not influence the thresholds of the instabilities. Its influence on the nonlinear behavior of stationary periodic patterns is among other things discussed in the next section.

#### 4 Nonlinear analysis of the orientational instability

The amplitude of the linear solution in Eq. (19) is limited by the terms in Eqs. (15) that are nonlinear with respect to  $\tilde{\rho}$  and  $\mathbf{t}$ . Here we investigate the weakly nonlinear behavior beyond the orientational instability, i.e. in the region referred to as  $O$  in Fig. 2 where  $\rho_c < \rho_0 < \rho_d$  holds. This can be done numerically as exemplified in the next section and even analytically if  $\rho_0$  is not immoderately beyond  $\rho_c$  defined in (25): for a supercritical bifurcation, the amplitude of the mode initially growing with  $\sigma_I(k)$  is small immediately above threshold and may be determined in this range by a perturbative analysis, the so-called amplitude equation [28], whose derivation is sketched in appendix D.

The generic form of amplitude equations depends on the preferred pattern beyond a stationary supercritical bifurcation. In two spatial dimensions the pattern is either spatially periodic in one direction (stripes), in two (squares/rectangles) or in three directions (hexagonal patterns) [28]. Numerical simulations of the basic equations (15) indicate, as described in Sec. 5, that stripe and square patterns are favored immediately above the threshold of the orientational instability. Moreover, hexagonal structures are not driven in this system due to the overall up-down symmetry of Eqs. (15) with respect to  $\mathbf{t}$ , c.f. appendix D as well.

Square patterns at threshold may be described analytically by a superposition of two linear modes (i.e. stripes) with orthogonal wave numbers which can be chosen without restriction as  $\mathbf{k}_1 = (k_c, 0)$  and  $\mathbf{k}_2 = (0, k_c)$  with  $k_c$  given by Eq. (26) leading to the ansatz

$$\mathbf{w}_1 = \begin{pmatrix} \rho_1 \\ t_{1x} \\ t_{1y} \end{pmatrix} = \begin{pmatrix} 0 \\ X \\ 0 \end{pmatrix} e^{ik_c x} + \begin{pmatrix} 0 \\ 0 \\ Y \end{pmatrix} e^{ik_c y} + c.c., \quad (27)$$

where *c.c.* means the complex conjugate. In a small neighborhood of the threshold  $\rho_c$ , measured by the dimension-

less control parameter

$$\varepsilon = \frac{\rho_0 - \rho_c}{\rho_c}, \quad (28)$$

the time-dependent amplitudes  $X(t)$  and  $Y(t)$  of the square pattern are determined by two generic coupled nonlinear equations, the so-called amplitude equations [32,28]

$$\tau_0 \partial_t X = \varepsilon X - g_1 |X|^2 X - g_2 |Y|^2 X, \quad (29a)$$

$$\tau_0 \partial_t Y = \varepsilon Y - g_1 |Y|^2 Y - g_2 |X|^2 Y. \quad (29b)$$

The coefficients  $\tau_0$ ,  $g_1$  and  $g_2$  are derived in appendix D. The specific system under consideration enters into the description only in these coefficients via the parameters of the basic equations (15), namely  $\alpha$ ,  $D_r$  and  $\gamma$ , while Eqs. (29) are universal for a whole symmetry class of pattern forming systems.

Apart from the trivial solution  $X_0 = Y_0 = 0$ , reflecting the stable homogeneous system, the coupled amplitude equations (29) have also stationary finite amplitude solutions. These are at first

$$X_0 = \pm \sqrt{\frac{\varepsilon}{g_1}}, \quad Y_0 = 0, \quad (30a)$$

$$X_0 = 0, \quad Y_0 = \pm \sqrt{\frac{\varepsilon}{g_1}}, \quad (30b)$$

which correspond according to Eq. (27) to stripes periodic either in  $x$ - or in  $y$ -direction. Secondly, there is the stationary solution of equal amplitudes

$$X_0 = Y_0 = \pm \sqrt{\frac{\varepsilon}{g_1 + g_2}}, \quad (31)$$

which constitutes a square pattern. In real space, this square pattern in terms of the components of the vector field  $\mathbf{t}(\mathbf{r}, t)$  resembles the structures which are called asters and found in numerous experiments [8] as will become clear from the simulation pictures in Sec. 5.

As summarized in appendix E, by a linear stability analysis of the (nonlinear) stationary solutions given by Eqs. (30) and (31) one finds stable stripes as the preferred solution in the range  $g_2 > g_1 > 0$  of the nonlinear coefficients. In the parameter range  $|g_2| < g_1$  the square pattern is preferred [32].

These criteria for  $g_1$  and  $g_2$  may be translated according to their parameter dependence into the  $D_r$ - $\alpha$  plane, as shown in Fig. 3 with the nonlinear contributions of the rotational current neglected at first, i.e.  $\gamma = 0$ . The analytic calculations presented here are valid below the solid line in Fig. 3, since above the density instability takes place. The dotted line corresponds to the condition  $g_1 = g_2 > 0$  which separates the range of stable squares from stable stripe solutions. Along the dash-dotted line in Fig. 3 the bifurcation from the homogeneous basic state to the stripe pattern changes its behavior from a supercritical (below) to a subcritical one (above), so the expansion method is no more effective.

Nonlinear effects of the rotational diffusion and the active rotational current are described by the last term

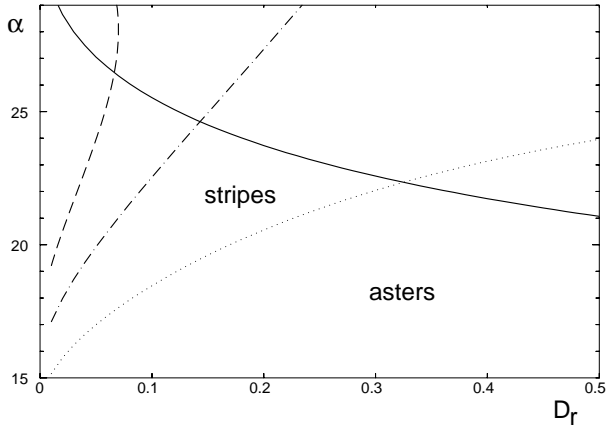


**Fig. 3.** The stability regions of stripes and asters are shown as calculated by the amplitude expansion method. The two critical densities  $\rho_c$  and  $\rho_d$  coincide along the solid line and beyond it instabilities with respect to density modulations are preferred not included in our present nonlinear analysis. The dotted line is given by  $g_1 = g_2$  and separates the range of stable square patterns (asters) from the range of stable stripe patterns. Along the dash-dotted line one has  $g_1 = 0$  and the bifurcation to stripes changes from supercritical (below) to a subcritical one (beyond). Between the dashed line, which is determined by  $g_1 = -g_2$ , and the dash-dotted line asters can still exist but are unstable while the amplitudes of stripes cannot be determined by our lowest order expansion. Beyond the dashed line, also asters bifurcate subcritical.

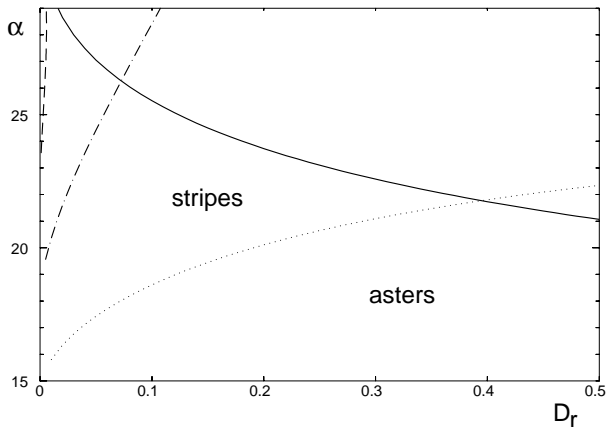


**Fig. 4.** The same diagram as in Fig. 3 but here the nonlinear contributions of rotational diffusion and active rotational currents, c.f. Eq. (10), are taken into account with  $\gamma = \alpha$ . The region of stable stripes considerably broadens while the regions of subcritical bifurcations are moved to higher  $\alpha$  and lower  $D_r$  values.

in Eq. (15b). Since they make no contribution to the linear operator, they can only change the pattern selection, i.e. the stability regions of the nonlinear solutions. Taking them into account, the bifurcation behavior from the homogeneous basic state is changed as shown in Fig. 4 for  $\gamma = \alpha$ , showing that these effects enlarge the range of stable stripe patterns in the  $D_r$ - $\alpha$  plane.

One may complement this outline of the bifurcation behavior by a discussion of the two decisive model parameters, namely  $\alpha$  and  $D_r$ , and analytical estimates for them. Simple models for motor proteins [2, 16, 17, 26] imply that the rate  $\alpha$  of the translational active transport grows linearly with the active motor density  $\rho_m$  and with the length of the filaments, i.e.  $\alpha \propto \rho_m l$ . Hence this rate can be controlled by the cell in the most effective way by the degree of motor activity (i.e. by regulating the ATP concentration) as well as on a much larger timescale by the density of the motors and the filament length.

For the rotational and translational diffusion coefficients in a *dilute solution*, calculations taking the hydrodynamic interaction into account [19] propose the analytical expressions

$$D_r = \frac{3 \ln(l/b)}{\pi \eta l^3}, \quad D_{\parallel} = \frac{\ln(l/b)}{2\pi \eta l}. \quad (32)$$

In our scaled units this means  $D'_r = \frac{l^2}{D_{\parallel}} D_r = 6$ , lying far in the range of squares (asters).

For *semi-dilute solutions* one obtains in a similar manner  $D_r = 6 D_{\parallel} / (l^2 (1 + c_r \rho')^2)$  or

$$D'_r = \frac{l^2}{D_{\parallel}} D_r = \frac{6}{(1 + c_r \rho')^2} \quad (33)$$

in scaled units, where  $c_r \simeq 1$  is a geometry factor from a tube model calculation. Since stripes or bundle-like structures are stable for  $D'_r < 0.3$ – $0.4$ , c.f. Figs. 3 and 4, one needs a rather high (but possible) filament density for such a one-dimensional ordering.

According to these estimates asters are the most likely pattern occurring above a stationary bifurcation in dilute or semi-dilute two-dimensional motor-filament-systems. For bundle-like structures to emerge rather high filament densities are needed, which is physically intuitive from the overlap nature of all the interactions, namely excluded volume and motor-induced filament-filament interaction.

## 5 Results of numerical simulations

Besides the weakly nonlinear analysis described in the previous section, the basic equations (15) have been solved numerically in order to check the validity range of the perturbation analysis and further explore the solution space. For this purpose a Fourier Galerkin pseudo-spectral method has been used imposing periodic boundary conditions on the system.

Since the validity range of the amplitude expansion with respect to the control parameter  $\varepsilon$  is not known a priori, in Fig. 5 we compare the amplitude of a stripe solution as obtained by a numerical solution of the basic equations (15) with the analytical results given by Eq. (30). Close to threshold there is nearly perfect agreement between both approaches. However the validity range of the amplitude equations is actually restricted to a range below  $\varepsilon \sim 0.006$  for the parameters used in Fig. 5. Around

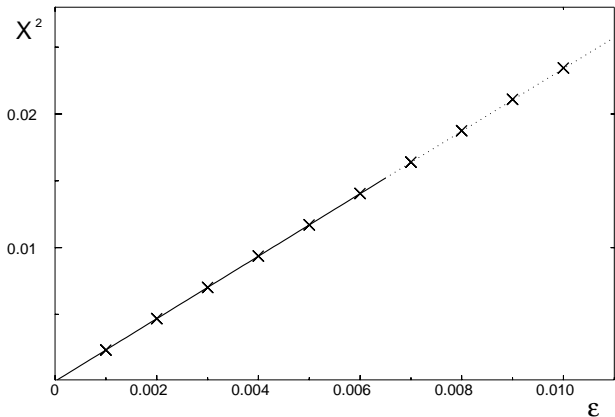


**Fig. 5.** A comparison of the amplitude of a stripe solution as obtained in simulations (crosses) with the analytical calculation  $X_0 = \pm(\varepsilon/g_1)^{1/2}$  as given by Eq. (30) is shown. The agreement remains well for higher values of  $\varepsilon$ , but in the range between  $\varepsilon \simeq 0.006-0.007$  a secondary bifurcation takes place rendering the high- $\varepsilon$  solutions unstable. Parameters are  $D_r = 0.5$ ,  $\alpha = 21$  and  $\gamma = 0$ .

this value a secondary instability takes place, which is not taken into account in the perturbation expansion. The numerical simulations show that beyond this secondary instability a pronounced accumulation of the filaments to densities even higher than  $\rho_{IN}$  appear accompanied with high alternating orientations. These solutions are numerically stable but nevertheless in an invalid range of our model since the nematic order parameter, c.f. Eqs. (11), has been neglected in the moment expansion which is not legitimate anymore – so we reject showing pictures here.

In addition to the validity range with respect to  $\varepsilon$ , one may also confirm numerically the stability of the nonlinear solutions as predicted in Fig. 3 by the weakly nonlinear analysis. As an example, we start with a square solution as shown in Fig. 6a) at the point  $\alpha = 21$  and  $D_r = 0.15$  in parameter space (and  $\varepsilon = 5 \cdot 10^{-4}$ ) belonging according to Fig. 3 to the region of stable stripe patterns. After a slight perturbation, the simulated temporal evolution in Fig. 6c) shows that only one of the initially equal amplitudes remains finite in the long time limit leading to the predicted stationary stripe pattern displayed in Fig. 6b). By several numerical runs we confirmed the analytically predicted stability diagrams in Figs. 3 and 4.

In the parameter range of stable asters, a vectorplot of the orientation field superposed on the color coded filament density is presented in Fig. 7. The filament orientation is indicated by arrows, the length being a measure of the degree of orientation. The density is high in the bright regions and low in the dark ones. At the right hand side in Fig. 7, one can spot an aster with arrows pointing radially from a center with lowered filament density opposing to an inverse aster top left with arrows pointing radially into the center (we remind the reader that periodic boundary conditions are imposed). The centers of the asters have lowered filament densities which can be explained by the nonlinear analysis: in the derivation of

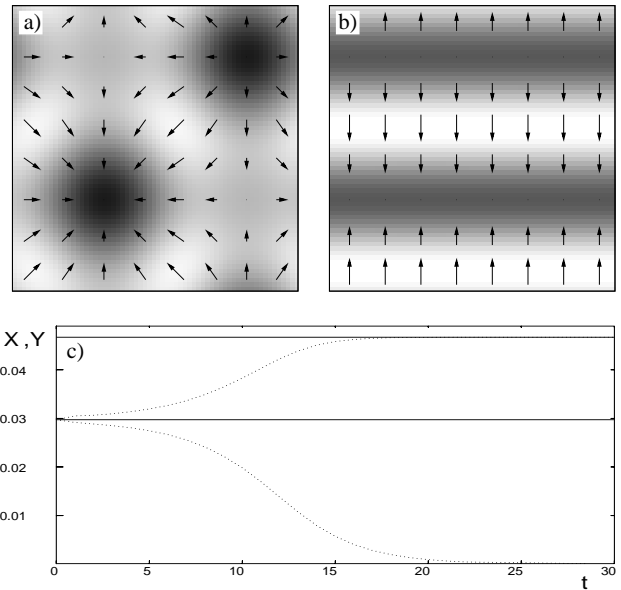


**Fig. 6.** A scenario is shown where a repetitive structure of asters as displayed in (a) is slightly disturbed at a point in parameter space where stripes are preferred, namely at  $\alpha = 21$  and  $D_r = 0.15$  ( and  $\varepsilon = 5 \cdot 10^{-4}$  ). In part (c) the solid lines correspond to the analytical values of the amplitudes  $X_s = Y_s = 0.0297$  for squares and  $X_r = 0.0467$  for stripes respectively while the dotted lines show how the amplitudes  $X$  and  $Y$  of the polar orientation components  $t_x$  and  $t_y$  evolve in time from the unstable square pattern to the stationary stripe solution in (b).

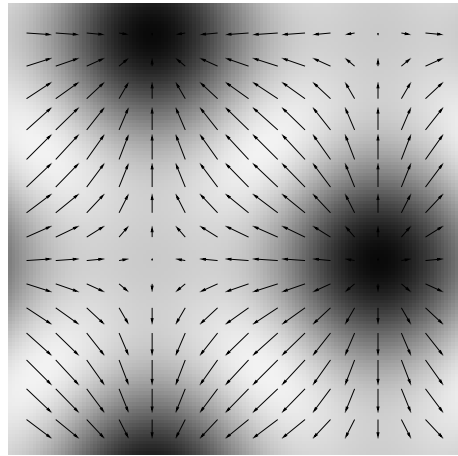


**Fig. 7.** A simulation of Eqs. (15) in the range of stable stationary asters is shown as a superposed plot of the orientation field (arrows) and the filament density (dark color coding low density, light color high density). Parameters are  $\alpha = 21$ ,  $D_r = 0.5$ ,  $\varepsilon = 5 \cdot 10^{-5}$ .

the amplitude equations in appendix D one can clearly see that the growing amplitudes of the orientation modulations excite higher density modes - which then limit the orientation amplitudes to render the system stable - and therefore in the center of an aster, where the orientation vanishes, there is no need for a high density. Both density



and the degree of orientation reach their maximum in between the asters and two saddle-like structures building up a square with the two opposing aster centers complete the repetitive structure of the pattern at threshold in the motor–filament–system.

## 6 Summary and conclusions

For a model of interacting biopolymers and motor proteins, a nonlinear competition between the formation of stripes and square patterns has been described for the first time. The model is based on a nonlinear (and nonlocal) Smoluchowski equation for the distribution function of rigid rods extended by active currents to account for the motor-mediated relative motion of the filaments. This equation can be approximated by a local equation of motion under the assumption that the spatial variations are small on the length scale of the filaments, which allows a gradient expansion [26]. However, this expansion has to be continued up to fourth order in the gradients as pointed out recently in order to reasonably evaluate the linear stability of the homogeneous filament distribution [27]. This expansion as well as the linear stability of the basic state are described comprehensively. The homogeneous state may become unstable with respect to density, orientational and nematic instabilities, but in different parameter ranges as shown in Fig. 2. The two crucial model parameters are the rate of active translational transport and the rotational diffusion coefficient which both can be regulated by the cell by creating filaments, motor proteins and the fuel ATP as discussed and estimated at the end of Sec. 4.

Our subsequent nonlinear analysis focuses on the orientational instability, which may be of high biological relevance for aster-like structures as in the mitotic spindle which have also been seen in *in vitro* systems recently [8,11]. This analysis is to a large extent analytically in terms of an amplitude expansion technique yielding two coupled equations, namely Eqs. (29), for the amplitudes of the spatial modulation of the orientational field in  $x$ - and  $y$ -direction. These two coupled equations determine the amplitudes of square (asters) and stripe patterns and they provide also the stability boundary between both solutions near threshold. Simulations with a spectral code and periodic boundary conditions confirmed these analytical results.

Estimates for the two model parameters  $\alpha$  and  $D_r$  of the basic equations (15), c.f. end of Sec. 4, suggest that asters are the most likely pattern occurring above a stationary bifurcation in dilute or semi-dilute two-dimensional motor–filament–systems. Stripes may be expected only for rather high filament densities which can be traced back to the overlap nature of both present interactions, namely excluded volume and motor-induced filament–filament interaction. Once again both the type of the pattern, i.e. asters or stripes, as well as its wavelength could be governed by the cell by creating filaments, motor proteins and ATP.

Experiments as described in Refs. [7,8,9] show that in a model system comprised of microtubules and a single

type of motor in a confined geometry asters may arise but are unstable to a vortex with motors rotating around the center, whereas in unconfined geometries, with increasing motor concentration, the arising patterns are vortices, mixtures of asters and vortices, asters and finally bundles of microtubules for high motor densities. This is in agreement with our calculations visualized in Fig. 3, as for moderate values of  $D_r$  the asters in our model become unstable against stripe formation for increasing  $\alpha$ , which is proportional to the (homogeneous) density of motors. Since we only considered periodic boundary conditions, we did not find vortices, which nevertheless may be possible if a confined geometry is simulated. In contrast to this good agreement with microtubule-motor systems, recent experiments on actin-myosin systems [11] showed that the models at hand can not be directly used in that case. But modifying the present model to account for ATP depletion and stable cross-linking of the filaments by inactive myosin complexes, it is even able to explain the different aster formation mechanism in actin [11,35].

The first attempt of describing patterns in microtubules and motors in Ref. [8] was done by a molecular dynamics simulation where asters and vortices could be reproduced. In a subsequent publication [12], the case of two types of motors walking on the filaments in opposite directions was investigated and a pattern referred to as a network of interconnected poles was obtained which is very similar to the pattern near threshold displayed in Fig. 7. A first macroscopic description of the problem was given in Ref. [14], where coarse-grained equations derived from a spin-like model displayed stripe patterns. Finally, in Ref. [15] equations for the motor density and a phenomenological vector field describing the polar orientation were proposed, which reproduced asters and, in a confined geometry, vortices, but were not able to describe stripe patterns. This can be traced back to the omission of an explicit equation for the filament density. More severely, as will be worked out in Ref. [35], in the model presented here linear couplings between the density and the orientation field via the active transport terms proportional to  $\beta$  lead to an oscillatory instability and propagating modes through the motor–filament–system, which cannot be described by Ref. [15] but should be highly relevant for vital processes like cell spreading on a substrate as measured for instance in Ref. [36].

Some experiments indicate that the spatially inhomogeneous distribution of the motor density may become a further relevant degree of freedom [37] and therefore should be taken into account for various purposes in future models. This degree of freedom in combination with stable crosslinking may also give rise to a different instability in actomyosin [11,35]. From the theoretical point of view it would be interesting to extend the moment expansion scheme one step further yielding an equation for the nematic order parameter tensor. This would allow to take also the effects of nematic order into account and to study its interplay with the polar orientation in the presence of motors, which may lead to an interesting model system of a new symmetry class.

## A Symmetries of the motor-mediated velocities

The explicit form of the motor-mediated translational and angular velocities, namely Eqs. (9) and (10), can be obtained by writing down the simplest terms fulfilling the conservation laws and symmetries of the system.

If one considers an interacting filament pair in the absence of external forces and torques, both momentum and angular momentum of the pair have to be conserved. Hence the motor-mediated translational and angular velocities,  $\mathbf{v} = \dot{\mathbf{r}} - \dot{\mathbf{r}}'$  and  $\boldsymbol{\omega} = \dot{\mathbf{u}} - \dot{\mathbf{u}}'$ , have to be odd under the transformation  $(\mathbf{r}, \mathbf{u}; \mathbf{r}', \mathbf{u}') \rightarrow (\mathbf{r}', \mathbf{u}'; \mathbf{r}, \mathbf{u})$ . Translational invariance leads to  $f(\mathbf{r}, \mathbf{r}') = f(\mathbf{r} - \mathbf{r}')$  for  $f = \mathbf{v}, \boldsymbol{\omega}$ . Together with the rotational invariance,  $\mathbf{v}$  has to be odd and  $\boldsymbol{\omega}$  even under the transformation  $(\mathbf{r} - \mathbf{r}'; \mathbf{u}, \mathbf{u}') \rightarrow (\mathbf{r}' - \mathbf{r}; -\mathbf{u}, -\mathbf{u}')$ . The simplest terms fulfilling the above conditions for  $\mathbf{v}$  are proportional to  $\mathbf{r} - \mathbf{r}'$  or  $\mathbf{u} - \mathbf{u}'$  and for  $\boldsymbol{\omega}$  proportional to  $\mathbf{u} \times \mathbf{u}'$ . One can thus write down [26]

$$\mathbf{v}(\mathbf{r} - \mathbf{r}', \mathbf{u}, \mathbf{u}') = \frac{\alpha}{2} \frac{\mathbf{r} - \mathbf{r}'}{L} \frac{1 + \mathbf{u} \cdot \mathbf{u}'}{|\mathbf{u} \times \mathbf{u}'|} + \frac{\beta}{2} \frac{\mathbf{u}' - \mathbf{u}}{|\mathbf{u} \times \mathbf{u}'|}, \quad (34)$$

$$\boldsymbol{\omega}(\mathbf{u}, \mathbf{u}') = \gamma (\mathbf{u} \cdot \mathbf{u}') \frac{\mathbf{u} \times \mathbf{u}'}{|\mathbf{u} \times \mathbf{u}'|}. \quad (35)$$

The term proportional to  $\alpha$  is made orientation-dependent (it could be generalized by allowing two different prefactors) and the plus sign favours parallel alignment. In the term proportional to  $\gamma$ , spatial dependence has been neglected and the prefactor  $\mathbf{u} \cdot \mathbf{u}'$  models the tendency of motors to bind on two filaments which share an angle smaller than  $\frac{\pi}{2}$ . The common factor  $|\mathbf{u} \times \mathbf{u}'|^{-1}$  is just a normalization to the interaction volume.

## B The gradient expansion of the interaction integrals

The excluded volume interactions, c.f. Eq. (6), as well as the motor induced rod-rod interaction, c.f. Eqs. (8), are defined by overlap integrals. Hence the equation of motion (2) for the probability distribution function  $\Psi(\mathbf{r}, \mathbf{u})$  is nonlocal and its solution is exceedingly difficult. Assuming that spatial variations are small on the length scale of a filament, in order to deal with a local equation one can perform a systematic expansion of the integrals with respect to gradients of the probability distribution function, as described in this appendix.

The interaction kernel given by Eq. (7) can be expressed in terms of Straley coordinates [33], which in two dimensions are defined by

$$\mathbf{r} - \mathbf{r}' = \mathbf{u}\zeta + \mathbf{u}'\eta, \quad (36)$$

with the parameter constraint  $-L/2 < \zeta, \eta < L/2$  ( $L$  the filament length) and the Jacobian  $|\mathbf{u} \times \mathbf{u}'|$ . Thus the excluded volume interaction, namely Eq. (6), is determined

by the four dimensional integral

$$V_{ex}(\mathbf{r}, \mathbf{u}) = \int d\mathbf{u}' \int d\mathbf{r}' \int_{-L/2}^{L/2} d\zeta \int_{-L/2}^{L/2} d\eta |\mathbf{u} \times \mathbf{u}'| \delta(\mathbf{r} - \mathbf{r}' + \mathbf{u}\zeta + \mathbf{u}'\eta) \Psi(\mathbf{r}', \mathbf{u}'), \quad (37)$$

which may be approximated by a Taylor series expansion of the  $\delta$ -function with respect to  $\eta$  and  $\zeta$ .<sup>2</sup> Performing the  $\eta$  and  $\zeta$  integration one finally obtains

$$V_{ex}(\mathbf{r}, \mathbf{u}) = L^2 \int d\mathbf{u}' |\mathbf{u} \times \mathbf{u}'| \left[ 1 + \frac{L^2}{24} \left\{ (\mathbf{u} \cdot \partial_{\mathbf{r}})^2 + (\mathbf{u}' \cdot \partial_{\mathbf{r}})^2 \right\} \right] \Psi(\mathbf{r}, \mathbf{u}'), \quad (38)$$

where terms up to second order in the spatial derivatives have been taken into account. The prefactor  $L^2$  reflects the two-dimensional excluded volume.

By a similar procedure, the contribution to the active current proportional to  $\alpha$  can be evaluated as

$$J_t^a = -\frac{\alpha L^3}{24} \partial_i \int d\mathbf{u}' \Psi(\mathbf{r}, \mathbf{u}) (1 + \mathbf{u} \cdot \mathbf{u}') \cdot \left\{ u_i (\mathbf{u} \cdot \partial_{\mathbf{r}}) \left[ 1 - \frac{L^2}{16} \left( \frac{2}{5} (\mathbf{u} \cdot \partial_{\mathbf{r}})^2 + \frac{2}{3} (\mathbf{u}' \cdot \partial_{\mathbf{r}})^2 \right) \right] + u'_i (\mathbf{u}' \cdot \partial_{\mathbf{r}}) \left[ 1 - \frac{L^2}{16} \left( \frac{2}{5} (\mathbf{u}' \cdot \partial_{\mathbf{r}})^2 + \frac{2}{3} (\mathbf{u} \cdot \partial_{\mathbf{r}})^2 \right) \right] \right\} \Psi(\mathbf{r}, \mathbf{u}'). \quad (39)$$

One should note that due to the  $\zeta, \eta$ -integrations, odd powers of  $\partial_{\mathbf{r}}$  vanish in both expressions, which is the mathematical reason underlying the rotational symmetry of Eqs. (15).

## C The moment expansion method

The method for deriving the coupled Eqs. (15) for the density and the orientation field of the filaments from the underlying Smoluchowski-equation, Eq. (2), is similar to the calculations presented in Ref. [38], where it has been used to obtain equations describing the initial stage of spinodal decomposition during the isotropic-nematic transition of a three-dimensional hard-rod fluid. In both cases, the starting point is an approximate description of the probability distribution function  $\Psi(\mathbf{r}, \mathbf{u}, t)$  by its moments, but in contrast to a usual liquid crystal as considered in Ref. [38], now the rods are polar with respect to the motor action. Thus the  $\pm \mathbf{u}$ -symmetry is broken and the first moment, namely the filament orientation field  $\mathbf{t}$ , does not vanish here and cannot be omitted. Hence one has to approximate  $\Psi(\mathbf{r}, \mathbf{u}, t)$  by its first two moments,

$$\Psi(\mathbf{r}, \mathbf{u}, t) \simeq \frac{1}{2\pi} (\rho(\mathbf{r}, t) + 2\mathbf{u} \cdot \mathbf{t}(\mathbf{r}, t)) , \quad (40)$$

<sup>2</sup> Equivalently, after performing the  $\mathbf{r}'$ -integration the shifted distribution function  $\Psi(\mathbf{r} + \mathbf{u}\zeta + \mathbf{u}'\eta)$  may be expanded.

with the filament density  $\rho(\mathbf{r}, t)$  and the orientation field  $\mathbf{t}(\mathbf{r}, t)$ , c.f. Eqs. (11).

The validity of the representation in Eq. (40) can be seen immediately by using it to evaluate the first moments which correctly yields  $\int d\mathbf{u} \Psi(\mathbf{r}, \mathbf{u}) = \rho(\mathbf{r})$  and  $\int d\mathbf{u} \mathbf{u} \Psi(\mathbf{r}, \mathbf{u}) = \mathbf{t}(\mathbf{r})$ . Inserting the currents as defined by Eqs. (3) and (8) as well as applying the gradient expansion given in appendix B, then an integration of Eq. (2) by  $\int d\mathbf{u}$  and  $\int d\mathbf{u} \mathbf{u}$  yields two evolution equations for  $\rho(\mathbf{r}, t)$  and  $\mathbf{t}(\mathbf{r}, t)$  respectively, as given by Eqs. (15).

The remaining integrals involved are merely orientational averages. If one defines

$$\langle A(\mathbf{u}) \rangle_{\mathbf{u}} = \int \frac{d\mathbf{u}}{2\pi} A(\mathbf{u}) = \int_0^{2\pi} \frac{d\theta}{2\pi} A(\theta) , \quad (41)$$

where  $\theta$  parameterizes the unit vector  $\mathbf{u}$  in two dimensions, the following formulas are useful and easily proven: All mean values depending on odd powers of  $\mathbf{u}$  vanish as well as the mean values of any product of  $|\mathbf{u} \times \mathbf{u}'|$  and odd powers of  $\mathbf{u}$  or  $\mathbf{u}'$ , since  $|\mathbf{u} \times \mathbf{u}'| = \sqrt{1 - (\mathbf{u} \cdot \mathbf{u}')^2}$  contains only even powers of  $\mathbf{u}, \mathbf{u}'$ . For the even powers one gets

$$\langle u_\alpha u_\beta \rangle_{\mathbf{u}} = \frac{1}{2} \delta_{\alpha\beta} , \quad (42)$$

$$\langle u_\alpha u_\beta u_\mu u_\nu \rangle_{\mathbf{u}} = \frac{1}{8} (\delta_{\alpha\beta} \delta_{\mu\nu} + \delta_{\alpha\mu} \delta_{\beta\nu} + \delta_{\alpha\nu} \delta_{\beta\mu}) \quad (43)$$

and

$$\langle u_\alpha u_\beta u_\mu u_\nu u_\sigma u_\tau \rangle_{\mathbf{u}} = \frac{1}{48} \sum_{\mathcal{P}} \delta_{ij} \delta_{kl} \delta_{mn} , \quad (44)$$

where  $\mathcal{P}$  means all the permutations of  $\{\alpha, \beta, \mu, \nu, \sigma, \tau\}$  generating different index combinations of the Kronecker delta product. Furthermore one needs

$$\langle |\mathbf{u} \times \mathbf{u}'| \rangle_{\mathbf{u}'} = \int \frac{d\theta'}{2\pi} |\sin(\theta - \theta')| = \frac{2}{\pi} \quad (45)$$

and

$$\langle |\mathbf{u} \times \mathbf{u}'| u'_\alpha u'_\beta \rangle_{\mathbf{u}'} = -\frac{2}{3\pi} (u_\alpha u_\beta - 2\delta_{\alpha\beta}) . \quad (46)$$

The operator of rotational diffusion in two dimensions as given by Eq. (5) can be expressed as

$$[\mathcal{R}]_i = [\mathbf{u} \times \partial_{\mathbf{u}}]_i = \delta_{i3} (u_1 u'_2 - u_2 u'_1) \quad (47)$$

and for the rotational terms, the following partial integration formula

$$\langle A(\mathbf{u}) \mathcal{R} [B(\mathbf{u})] \rangle_{\mathbf{u}} = -\langle \mathcal{R} [A(\mathbf{u})] B(\mathbf{u}) \rangle_{\mathbf{u}} \quad (48)$$

is crucial to simplify calculations.

As an example, we calculate a rather simple term, namely the excluded volume contribution to the equation of motion for the filament density  $\rho$ , c.f. (15a), which is

proportional to  $D_{\parallel}$  and second order in spatial derivatives. So we have to deal with

$$D_{\parallel} \int d\mathbf{u} u_i u_j \partial_i \left( \Psi(\mathbf{u}) \partial_j L^2 \int d\mathbf{u}' |\mathbf{u} \times \mathbf{u}'| \Psi(\mathbf{u}') \right) , \quad (49)$$

where spatial coordinates have been suppressed. Substituting the representation Eq. (40) twice and using the nomenclature introduced in Eq. (41), we have to calculate

$$\langle u_i u_j \partial_i ([\rho + 2u_k t_k] \partial_j \langle |\mathbf{u} \times \mathbf{u}'| [\rho + 2u'_l t_l] \rangle_{\mathbf{u}'} \rangle_{\mathbf{u}} . \quad (50)$$

The contributions  $u_k t_k, u'_l t_l$  vanish because of their oddness. Thus we are left with

$$\langle u_i u_j \partial_i (\rho \partial_j \langle |\mathbf{u} \times \mathbf{u}'| \rangle_{\mathbf{u}'} \rho) \rangle_{\mathbf{u}} \quad (51)$$

which can be simplified to

$$\frac{2}{\pi} \langle u_i u_j \rangle_{\mathbf{u}} \partial_i (\rho \partial_j \rho) = \frac{1}{\pi} \nabla \cdot (\rho \nabla \rho) \quad (52)$$

by using Eqs. (42) and (45).

## D Derivation of the amplitude equations

Here we describe the scheme for the derivation of the two coupled amplitude equations (29) from the three underlying nonlinear equations (15). First of all one assumes small values for the amplitudes  $X$  and  $Y$  of the spatially periodic deviations from the homogeneous basic state  $\rho_0$  and  $\mathbf{t} = 0$ . At threshold, i.e. at  $\rho_0 = \rho_c$  and for  $k_c$  as calculated in Eqs. (25) and (26), these deviations are either periodic in  $x$ - or in  $y$ -direction as described by the ansatz in Eq. (27).

Similar to Sec. 3, the nonlinear equations (15) may be rewritten in terms of the deviations  $\mathbf{w} = (\tilde{\rho}, t_x, t_y)$  from the basic state  $\mathbf{w}_0 = (\rho_0, 0, 0)$  as follows:

$$\partial_t \mathbf{w} = \mathcal{L}_0 \mathbf{w} + \mathbf{N}(\rho, \mathbf{t}) \quad (53)$$

$$\text{with } \mathbf{N}(\rho, \mathbf{t}) = \begin{pmatrix} \mathcal{N}_\rho(\rho, \mathbf{t}) \\ \mathcal{N}_x(\rho, \mathbf{t}) \\ \mathcal{N}_y(\rho, \mathbf{t}) \end{pmatrix} . \quad (54)$$

The linear operator is defined by Eq. (18) and the nonlinear operator  $\mathbf{N}$  includes all the nonlinear terms with respect to  $\tilde{\rho}$  and  $\mathbf{t}$  on the right hand sides of Eqs. (15).

Naturally, as the small expansion parameter the relative distance from the threshold,

$$\varepsilon = \frac{\rho_0 - \rho_c}{\rho_c} , \quad (55)$$

is chosen. Close to threshold the dynamics of the linear solution in Eq. (19) is slow and accordingly a slow time scale

$$T = \varepsilon t \quad (56)$$

is introduced allowing the time derivatives in Eqs. (15) to be replaced by

$$\partial_t \rightarrow \varepsilon \partial_T . \quad (57)$$

The solution  $\mathbf{w}$  is expanded with respect to powers of  $\varepsilon^{1/2}$

$$\mathbf{w} = \varepsilon^{1/2}\mathbf{w}_1 + \varepsilon\mathbf{w}_2 + \varepsilon^{3/2}\mathbf{w}_3 + \dots, \quad (58)$$

with  $\mathbf{w}_1$  as in Eq. (27), as are the nonlinearities

$$\mathbf{N} = \varepsilon\mathbf{N}_1 + \varepsilon^{3/2}\mathbf{N}_2 + \dots. \quad (59)$$

Sorting the contributions to Eq. (53) with respect to powers of  $\varepsilon$ , one ends up with the following hierarchy of equations

$$\varepsilon^{1/2} : \mathcal{L}_0\mathbf{w}_1 = 0, \quad (60a)$$

$$\varepsilon : \mathcal{L}_0\mathbf{w}_2 = -\mathcal{N}_\rho(\mathbf{t}_1)e_\rho, \quad (60b)$$

$$\varepsilon^{3/2} : \mathcal{L}_0\mathbf{w}_3 = \partial_T\mathbf{w}_1 - \mathcal{L}_2\mathbf{w}_1 - \sum_{i=x,y} \mathcal{N}_i(\rho_2, \mathbf{t}_1)e_i, \quad (60c)$$

that has to be solved successively. We have introduced  $e_\rho = (1, 0, 0)$ ,  $e_x = (0, 1, 0)$ ,  $e_y = (0, 0, 1)$  and

$$\mathcal{L}_2 = \begin{pmatrix} \mathcal{L}_{11}^{(2)} & 0 & 0 \\ 0 & \mathcal{L}_{22}^{(2)} & \mathcal{L}_{23}^{(2)} \\ 0 & \mathcal{L}_{32}^{(2)} & \mathcal{L}_{33}^{(2)} \end{pmatrix} \quad (61)$$

with

$$\begin{aligned} \frac{1}{\rho_0}\mathcal{L}_{11}^{(2)} &= \left(\frac{3}{2\pi} - \frac{\alpha}{24}\right)\Delta - \frac{19\alpha}{11520}\Delta^2, \\ \frac{1}{\rho_0}\mathcal{L}_{22}^{(2)} &= -\frac{\alpha}{96}(\Delta + 2\partial_x^2) - \frac{\alpha}{46080}(11\Delta^2 + 64\Delta\partial_x^2), \\ \frac{1}{\rho_0}\mathcal{L}_{23}^{(2)} &= -\frac{\alpha}{48}\partial_x\partial_y - \frac{\alpha}{720}\Delta\partial_x\partial_y. \end{aligned} \quad (62)$$

The remaining two matrix elements  $\mathcal{L}_{32}^{(2)}$  and  $\mathcal{L}_{33}^{(2)}$  follow from  $\mathcal{L}_{23}^{(2)}$  and  $\mathcal{L}_{22}^{(2)}$  by permuting  $\partial_x$  and  $\partial_y$ .

The equation in  $\mathcal{O}(\varepsilon^{1/2})$  is just the linear eigenvalue problem already discussed as Eq. (16) in Sec. 3, i.e. it is solved by  $\tilde{\rho}_1 = 0$  and

$$t_{1x} = X(T)e^{ik_c x} + c.c., \quad t_{1y} = Y(T)e^{ik_c y} + c.c. \quad (63)$$

describing the orientational fluctuations.

At the next order  $\mathcal{O}(\varepsilon)$ , the nonlinearity is only present in the density equation, while  $\mathcal{L}_0$  acting on the  $\mathbf{t}$ -subspace is nonsingular, leading to  $\mathbf{t}_2 = 0$ . The overall up-down symmetry of Eqs. (15) with respect to  $\mathbf{t}$  prohibits hexagonal structures as can be seen in this order in  $\varepsilon$ , where for hexagons to be driven a quadratic contribution in the equations that are linearly unstable, i.e. in the equations for the orientation fields  $t_x$  and  $t_y$  would be needed [31]. Inserting  $\mathbf{t}_1$  in  $\mathcal{N}_\rho(\mathbf{t}_1)$  yields an equation for  $\rho_2$ , whose solution is of the following form

$$\begin{aligned} \rho_2(X, Y) &= r_1 X^2 e^{2ik_x} + r_2 Y^2 e^{2iq_y} \\ &+ r_3 XY e^{i(k_x + q_y)} + r_4 XY^* e^{i(k_x - q_y)} + c.c. \end{aligned} \quad (64)$$

with  $r_i = r_i(\alpha, D_r, \gamma)$  for  $i = 1, \dots, 4$ . Here one can see that the coupling of the orientational field to the density is crucial for the physical stability of the system, since the

density  $\rho_2$  is responsible for the saturation of the amplitudes in the equation of the next order  $\varepsilon^{3/2}$ , c.f. Eq. (60c), while  $\mathbf{t}_2 = 0$  and thus  $\mathbf{t}$  can not limit the amplitudes.

Instead of solving Eq. (60c) at the order  $\mathcal{O}(\varepsilon^{3/2})$ , one can use Fredholm's alternative, which states that for Eq. (60c) having solutions, there must not exist terms on its right hand side that lie in the kernel of  $\mathcal{L}_0$ , i.e. no contributions proportional to the critical modes  $\exp(ik_c x)$ ,  $\exp(ik_c y)$ . Collecting the prefactors of these respective modes, one gets the two equations (29), with analytical but lengthy expressions for  $\tau_0, g_1, g_2$  as functions of  $\alpha, D_r$  and  $\gamma$ .

## E Existence and stability of the nonlinear stripe and square state

The range of existence as well as the range of linear stability for roll solutions and for the squares can be easily investigated in terms of the amplitude equations. Stationary single amplitude solutions as given in Eqs. (30) exist beyond threshold, i.e. for  $\varepsilon > 0$ , only when  $g_1 > 0$  holds. The amplitudes for a stationary square, Eq. (31), follow from Eqs. (29) assuming equal amplitudes

$$|X| = |Y| = \sqrt{\frac{\varepsilon}{g_1 + g_2}}. \quad (65)$$

Obviously, squares exist beyond threshold only in the parameter range  $g_1 + g_2 > 0$ .

**Linear stability.** For small perturbations  $\delta X$  and  $\delta Y$  of the stripe and square solutions respectively, one obtains by the ansatz  $X = X_0 + \delta X$  and  $Y = Y_0 + \delta Y$  and linearizing Eqs. (29) with respect to  $\delta X$  and  $\delta Y$  two coupled equations in both perturbations. Those may be solved by the mode ansatz  $(\delta X, \delta Y) \sim (\delta \tilde{X}, \delta \tilde{Y})e^{\sigma t}$  leading to a second order polynomial in  $\sigma$  providing two eigenvalues. One of them is always negative while the second is either

$$\sigma_r = \varepsilon \frac{g_1 - g_2}{g_1} \quad (66)$$

for rolls or

$$\sigma_s = 2\varepsilon \frac{g_2 - g_1}{g_1 + g_2} \quad (67)$$

for squares.

Thus stripes or squares are stable if  $\sigma_r$  or  $\sigma_s$  is negative, respectively. Accordingly stripes are the preferred solution in the range of the nonlinear coefficients  $g_2 > g_1 > 0$ , while in the parameter range  $|g_2| < g_1$  the square patterns are preferred [32]. Since the nonlinear coefficients  $g_1$  and  $g_2$  are functions of the rate of active translational transport  $\alpha$  and of the rotational diffusion coefficient  $D_r$ , we are able to plot the stability ranges of the patterns as depicted in Figs. 3, 4.

## References

1. B. Alberts *et al.*, *Molecular Biology of the Cell* (Garland Publishing, New York, 2001).
2. J. Howard, *Mechanics of Motor Proteins and the Cytoskeleton* (Sinauer, Sunderland, 2001).
3. A. Hyman and E. Karsenti, *Cell* **45**, 329 (1986).
4. E. Karsenti and I. Vernos, *Science* **294**, 543 (2001).
5. D. Pantaloni, C. LeClainche, and M. F. Carlier, *Science* **292**, 1502 (2001).
6. A. B. Verkhovskiy, T. M. Svitkina, and G. G. Borisy, *Curr. Bio.* **9**, 11 (1999).
7. R. Urrutia *et al.*, *Proc. Natl. Acad. Sci. USA* **88**, 6701 (1991).
8. F. J. Nedelec, T. Surrey, A. C. Maggs, and S. Leibler, *Nature* **389**, 305 (1997).
9. T. Surrey *et al.*, *Proc. Natl. Acad. Sci. USA* **95**, 4293 (1998).
10. D. Humphrey *et al.*, *Nature* **416**, 413 (2002).
11. D. Smith *et al.*, *Molecular motors in cells: A rapid switch of biopolymer organization*, in preparation, 2004.
12. T. Surrey, F. Nedelec, S. Leibler, and E. Karsenti, *Science* **292**, 116 (2001).
13. F. Nédélec, *J. Cell Bio.* **158**, 1005 (2002).
14. B. Bassetti, M. C. Lagomarsino, and P. Jona, *Eur. Phys. J. B* **15**, 483 (2000).
15. H. Y. Lee and M. Kardar, *Phys. Rev. E* **64**, 056113 (2001).
16. H. Nakazawa and K. Sekimoto, *J. Physiol. Soc. Japan* **65**, 2404 (1996).
17. K. Kruse and F. Jülicher, *Phys. Rev. Lett.* **85**, 1778 (2000).
18. K. Kruse, A. Zumdieck, and F. Jülicher, *Europhys. Lett.* **64**, 716 (2003).
19. M. Doi and S. F. Edwards, *The Theory of Polymer Dynamics* (Clarendon Press, Oxford, 1986).
20. L. Onsager, *Ann. N.Y. Acad. Sci.* **51**, 627 (1949).
21. P. G. de Gennes and J. Prost, *The Physics of Liquid Crystals* (Clarendon, Oxford, 1993).
22. Z. Y. Chen, *Macromolecules* **26**, 3419 (1993).
23. A. L. Hitt, A. R. Cross, and J. R. C. Williams, *J. Bio. Chem.* **265**, 1639 (1990).
24. A. Suzuki, T. Maeda, and T. Ito, *Biophys. J.* **59**, 25 (1991).
25. F. Ziebert and W. Zimmermann, *Phys. Rev. E* **70**, 022902 (2004).
26. T. Liverpool and M. Marchetti, *Phys. Rev. Lett.* **90**, 138102 (2003).
27. F. Ziebert and W. Zimmermann, *Phys. Rev. Lett.* **93**, 159801 (2004).
28. M. C. Cross and P. C. Hohenberg, *Rev. Mod. Phys.* **65**, 851 (1993).
29. A. C. Newell, T. Passot, and J. Lega, *Ann. Rev. Fluid Mech.* **25**, 399 (1992).
30. P. Manneville, *Dissipative Structures and Weak Turbulence* (Academic Press, London, 1990).
31. S. Ciliberto *et al.*, *Phys. Rev. Lett.* **65**, 2370 (1990).
32. L. A. Segel, *J. Fluid Mech.* **21**, 359 (1965).
33. J. P. Straley, *Phys. Rev. A* **8**, 2181 (1973).
34. F. Nédélec and T. Surrey, *C. R. Acad. Sci. Paris S. IV* **6**, 841 (2001).
35. F. Ziebert and W. Zimmermann, in preparation, 2004.
36. H.-G. Döbereiner *et al.*, *Phys. Rev. Lett.* **93**, 108105 (2004).
37. F. Nédélec, T. Surrey, and A. C. Maggs, *Phys. Rev. Lett.* **86**, 3192 (2001).
38. T. Shimada, M. Doi, and K. Okano, *J. Chem. Phys.* **88**, 7181 (1988).